IEEE Access
Multidisciplinary ⋮ Rapid Review ⋮ Open Access Journal

Received 9 June 2024, accepted 26 June 2024, date of publication 1 July 2024, date of current version 9 July 2024.

Digital Object Identifier 10.1109/ACCESS.2024.3421614

RESEARCH ARTICLE

Single-/Dual-Band Bandpass-to-Bandstop Filters With Center Frequency Tunability

ALI KURSAD GORUR[1], (Member, IEEE), AND DIMITRA PSYCHOGIOU[2,3], (Senior Member, IEEE)
[1]Department of Electrical and Electronics Engineering, Nevşehir Hacı Bektaş Veli University, 50300 Nevşehir, Türkiye
[2]School of Engineering, University College Cork, Cork, T12 K8AF Ireland
[3]Tyndall National Institute, Cork, T12 R5CP Ireland

Corresponding author: Ali Kursad Gorur (akursadgorur@hotmail.com)

ABSTRACT This paper reports on the design and experimental validation of a new class of frequency-tunable filters with switchable bandpass-to-bandstop transfer function characteristics. Single- and dual-band filter topologies are developed by coupling dual-mode loop resonators (DMLRs) to the feedline between the RF input and output ports of the filter. The bandpass-to-bandstop reconfigurability is realized by adding/removing an in-parallel cascaded thru line using single pole double throw (SPDT) switches. Center frequency tunability is achieved by incorporating three varactor diodes in the DMLRs. For experimental validations purposes, two filters with single- and dual-band responses were implemented and tested and appear to be in a good agreement with the EM simulated performance. For the single-band bandpass-to-bandstop filter, the RF-measured tuning range for the bandpass mode of operation is 1.65-1.96 GHz, and for the bandstop mode or operation it is 1.68-1.93 GHz. The dual-band bandpass-to-bandstop filter exhibits the RF-measured tuning ranges of 1.38-1.53 GHz for the first passband and 1.82-2.08 GHz for the second passband in the bandpass mode operation. The minimum insertion loss varies between 3.3 and 6.8 dB for the first passband, whereas it is between 2.2 and 4.7 dB in the second passband. The RF-measured tuning ranges in its bandstop mode of operation were measured between 1.35-1.47 GHz and 1.75-2.01 GHz.

INDEX TERMS Bandpass filter, bandstop filter, single pole double throw (SPDT), tunable filter.

I. INTRODUCTION

Unprecedented developments in modern wireless communication systems such as in 5G, Internet-of-Space (IoS) and vehicle-to-vehicle (V2V) communications are increasingly calling for microwave RF components with increased functionality to support their multi-standard and multi-functional requirements. In this direction, tunable and reconfigurable microwave filters are highly desirable to replace the large number of RF-switched filter banks that currently limit the size and the power consumption of their RF transceivers and add complexity.

RF filters with reconfigurable number of passbands/stopbands, center frequency or bandwidth tunability have been demonstrated using alternative resonator technologies such as planar microstrip/CPW-type resonators [1], [2], [3], [4], [5], [6], [7], [8], [9], [10], [11], acoustic-wave resonators [12], [13], [14], [15], [16], [17], [18] and 3D cavities [19], [20], [21], [22], [23], [24]. Particularly, RF filters with bandpass-to-bandstop reconfigurable transfer functions are increasingly being sought to facilitate operation in interference dominated communication environments. As such, alternative bandpass-to-bandstop reconfigurable filters have been reported to date using different tuning technologies including micro-electromechanical system (MEMS) switches [25], [26], [27], [28], PIN diodes [29], [30], [31], [32], [33], [34], [35], [36], [37], [38], [39], [40], [41] and single pole double throw (SPDT) RF switches [42], [43], [44]. In [25] and [26], tunable single-band filters having two and four poles are demonstrated where MEMS switches facilitate the bandpass-to-bandstop reconfigurability and varactor diodes are used for center frequency tuning. Second- and third-order single-band bandpass-to-bandstop filters with frequency and bandwidth tunability are discussed in [27]. RF MEMS have also been used to materialize dual-band bandpass-to-bandstop filters with tunable bandwidth and

The associate editor coordinating the review of this manuscript and approving it for publication was Feng Lin.

reconfigurable transmission zeros, as for example the ones in [28]. However, they are frequency static.

PIN-diode based bandpass-to-bandstop filters are typically constructed by incorporating PIN diodes between the RF input and output ports. In [29], a single-band bandpass-to-bandstop filter has been demonstrated using parallel coupled resonators. However, neither its center frequency nor its bandwidth can be tuned. In yet another approach, frequency tunability is combined with bandpass-to-bandstop reconfigurability [30], [31], [32]. Multi-band bandpass-to-bandstop filters with tunable characteristics have also been reported, where tunability is obtained using trimmer capacitors [33]. In [34] another dual-band bandpass-to-bandstop filter has been demonstrated. Dual-band bandpass-to-bandstop filters with independently tunable center frequencies have been developed by incorporating PIN diodes in [35] and [36]. However, these filters suffer from the poor out-band performance in the bandstop mode of operation.

SPDT switches have been used to design bandpass-to-bandstop filters. In [42], a wideband filter with bandpass-to-bandstop reconfigurability is reported where quarter wavelength transmission lines are connected to a ring resonator by means of PIN diodes. Although high performance has been achieved at both of its bandpass and bandstop modes of operation, the filter is frequency static. In [43], SPDT switches were used together acoustic wave lumped element resonators to design single- and dual-band bandpass-to-bandstop filters. However, center frequency tunability can't be achieved. A bandpass-to-bandstop filter having center frequency tunability has been studied in [44], but it is limited to a single band.

Taking into consideration the aforementioned limitations, this manuscript reports on a new design approach to materialize single- and dual-band frequency-tunable filters with added bandpass-to-bandstop transfer function reconfigurability. The proposed filtering approach is based on dual-mode loop resonators (DMLRs). To achieve the bandpass-to-bandstop reconfigurability, an in-parallel connected transmission line is disconnected/ connected to the DMLR through a SPDT switch. Center frequency tuning is achieved by incorporating varactor diodes at the DMLR. The concept is applied to the realization of single-band and dual-band transfer functions. For experimental validation purposes, the prototypes we built and tested at L band. The proposed SPDT based dual-band bandpass-to-bandstop filters stand out due to having independently tuned center frequencies and good in-/out-band performance at both modes of operation. As compared to the dual-band tunable bandpass-to-bandstop filters introduced in [35] and [36], the proposed dual-band prototype exhibits better out-band return loss performance especially in the bandstop mode of operation. This work also includes the implementations for both of the single- and dual-band bandpass-to-bandstop filter prototypes. The proposed filters are like bandpass-to-bandstop RF filter banks due to the use of SPDT switches.

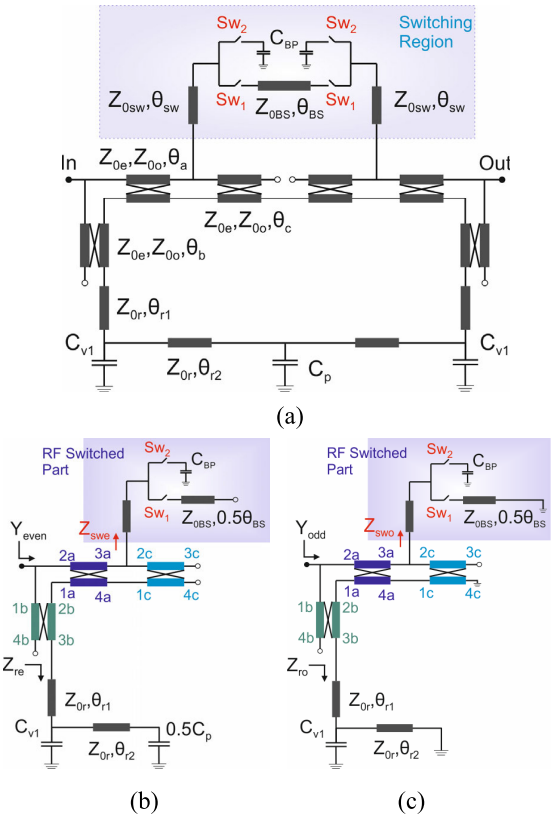

FIGURE 1. Circuit schematic of the single-band bandpass-to-bandstop filter with center frequency tunability. (a) Entire circuit. (b) Circuit equivalent under even mode excitation. (c) Circuit equivalent under odd mode excitation.

II. MATHEMATICAL ANALYSIS

The circuit schematic details of the single-band bandpass-to-bandstop filter concept are provided in Fig. 1(a). The DMLR is coupled to the RF input and output ports through feeding lines and an RF-switched transmission line is added in parallel to reconfigure its transfer function from bandpass to bandstop by activating/deactivating the RF switches Sw_1 and Sw_2. Specifically, the bandstop mode of operation can be obtained when Sw_1 is ON and Sw_2 is OFF, while the bandpass mode of operation can be obtained when Sw_1 is OFF and SW_2 is ON. Since the filter geometry has vertical symmetry, even and odd mode analysis can be performed using the even and odd mode circuit equivalents in Figs. 1(b) and 1(c). As it can be observed, the even mode resonant frequency can be controlled by C_{v1} and C_p, while the odd mode can be tuned by only changing C_{v1}. The input admittances of the even and the odd mode circuit equivalents, Y_{even} and Y_{odd}, can be found from the input impedance seen from the *1b* and *2a* ports of the coupled line sections using (1):

$$Y_{even} = Y_{odd} = \frac{I_{2a}}{V_{2a}} + \frac{I_{1b}}{V_{1b}} \tag{1}$$

where I_{1b}, V_{1b} and I_{2a}, V_{2a} are the currents and the voltages at the ports of *1b* and *2a*. It should be noted that the even and odd input admittances of Y_{even} and Y_{odd} can be calculated from the voltage-current relationships for three coupled sections of a, b, and c. Furthermore, the impedance matrices of the three

four-port coupled sections can be summarized as [45]:

$$Z^n_{11} = Z^n_{22} = Z^n_{33} = Z^n_{44} = \frac{-\mathrm{j}}{2}(\mathrm{Z_{0e}} + \mathrm{Z_{0o}})\cot(\theta_n) \quad (2a)$$

$$Z^n_{12} = Z^n_{21} = Z^n_{34} = Z^n_{43} = \frac{-\mathrm{j}}{2}(\mathrm{Z_{0e}} - \mathrm{Z_{0o}})\cot(\theta_n) \quad (2b)$$

$$Z^n_{13} = Z^n_{31} = Z^n_{24} = Z^n_{42} = \frac{-\mathrm{j}}{2}(\mathrm{Z_{0e}} - \mathrm{Z_{0o}})\csc(\theta_n) \quad (2c)$$

$$Z^n_{14} = Z^n_{41} = Z^n_{23} = Z^n_{32} = \frac{-\mathrm{j}}{2}(\mathrm{Z_{0e}} + \mathrm{Z_{0o}})\csc(\theta_n) \quad (2d)$$

where, $\mathrm{Z_{0e}}$ and $\mathrm{Z_{0o}}$ are the even and odd mode characteristic impedances of the coupled lines, and n represents the coupled sections a, b, and c in Figs. 1(a), (b) and (c).

Using the even mode half circuit model in Fig. 1(b), the voltages and the currents at the ports of the coupled sections can be specified as: $V_{1a} = V_{2b}$, $V_{2a} = V_{1b}$, $V_{3a} = V_{2c}$, $V_{4a} = V_{1c}$, $I_{1a} = -I_{2b}$, $I_{4a} = -I_{1c}$, $I_{2c} = -I_{3a} - \frac{V_{3a}}{Z_{swe}}$, $I_{4b} = I_{3c} = I_{4c} = 0$, and $V_{3b} = -I_{3b}Z_{re}$, where Z_{swe} and Z_{re} are the input impedances of the RF switched part and uncoupled section of the DMLR under even mode excitation. Z_{swe} can be expressed for the related switching path using (3):

$$Z_{swe,SW1} = j\mathrm{Z_{0sw}}\frac{-\mathrm{Z_{0BS}}\cot(\theta_{BS}) + \mathrm{Z_{0sw}}\tan(\theta_{sw})}{\mathrm{Z_{0sw}} + \mathrm{Z_{0BS}}\cot(\theta_{BS})\tan(\theta_{sw})} \quad (3a)$$

$$Z_{swe,SW2} = j\mathrm{Z_{0sw}}\frac{(\frac{-1}{\omega C_{BP}}) + \mathrm{Z_{0sw}}\tan(\theta_{sw})}{\mathrm{Z_{0sw}} + (\frac{1}{\omega C_{BP}})\tan(\theta_{sw})}. \quad (3b)$$

where $Z_{swe,SW1}$ is the input impedance of the switching path of $\mathrm{Sw_1}$ for the bandstop mode of operation and $Z_{swe,SW2}$ is the switching path of $\mathrm{Sw_2}$ for the bandpass mode of operation. Furthermore, the input impedance of the uncoupled sections of the DMLR, Z_{re}, can be found from (4):

$$Z_{re} = \mathrm{Z_{0r}}\frac{\mathrm{Z_{re1}} + j\mathrm{Z_{0r}}\tan(\theta_{r1})}{\mathrm{Z_{0r}} + j\mathrm{Z_{re1}}\tan(\theta_{r1})} \quad (4a)$$

$$Z_{re1} = \frac{\mathrm{Z_{re2}}}{1 + j\omega C_{v1}\mathrm{Z_{re2}}} \quad (4b)$$

$$Z_{re2} = \mathrm{Z_{0r}}\frac{1 - 0.5\omega C_p \mathrm{Z_{0r}}\tan(\theta_{r2})}{j0.5\omega C_p \mathrm{Z_{0r}} + j\tan(\theta_{r2})} \quad (4c)$$

Using, (2)-(4) as a reference, the input admittances seen from the *1b* and *2a* ports in (1) can be expressed as:

$$\frac{I_{2a}}{V_{2a}} = \frac{N_1L_4 - N_3L_2}{N_4L_2L_3 - N_2L_3L_4 + N_1N_4L_4 - N_2N_3L_4} \quad (5a)$$

$$\frac{I_{1b}}{V_{1b}} = \frac{N_1N_4 - N_2N_3}{N_4L_2L_3 - N_2L_3L_4 + N_1N_4L_4 - N_2N_3L_4} \quad (5b)$$

Its related parameters can be found from (6):

$$N_1 = Z^a_{11} - L_1 + M_3Z^a_{13} + M_1Z^a_{14} \quad (6a)$$

$$N_2 = Z^a_{12} + M_4Z^a_{13} + M_2Z^a_{14} \quad (6b)$$

$$N_3 = Z^a_{12} - L_3 + M_3Z^a_{14} + M_1Z^a_{13} \quad (6c)$$

$$N_4 = Z^a_{11} + M_4Z^a_{14} + M_2Z^a_{13} \quad (6d)$$

$$M_1 = \frac{K_1Z^a_{14} - K_3Z^a_{13}}{K_2K_3 - K_1K_4}, \quad M_2 = \frac{K_1Z^a_{13} - K_3Z^a_{14}}{K_2K_3 - K_1K_4} \quad (6e)$$

$$M_3 = \frac{K_4Z^a_{13} - K_2Z^a_{14}}{K_2K_3 - K_1K_4}, \quad M_4 = \frac{K_4Z^a_{14} - K_2Z^a_{13}}{K_2K_3 - K_1K_4} \quad (6f)$$

where:

$$L_1 = -Z^b_{11} + \frac{(Z^b_{14})^2}{Z^b_{11} + Z_{re}}, \quad L_2 = Z^b_{12} - \frac{Z^b_{13}Z^b_{14}}{Z^b_{11} + Z_{re}} \quad (7a)$$

$$L_3 = -Z^b_{12} + \frac{Z^b_{13}Z^b_{14}}{Z^b_{11} + Z_{re}}, \quad L_4 = Z^b_{11} - \frac{(Z^b_{13})^2}{Z^b_{11} + Z_{re}} \quad (7b)$$

$$K_1 = Z^a_{11} + \frac{Z^c_{11}Z_{swe}}{Z^c_{11} + Z_{swe}}, \quad K_2 = Z^a_{12} + \frac{Z^c_{12}Z_{swe}}{Z^c_{11} + Z_{swe}} \quad (7c)$$

$$K_3 = Z^a_{12} + Z^c_{12} - \frac{Z^c_{11}Z^c_{12}}{Z^c_{11} + Z_{swe}} \quad (7d)$$

$$K_4 = Z^a_{11} + Z^c_{11} - \frac{(Z^c_{12})^2}{Z^c_{11} + Z_{swe}} \quad (7e)$$

For the odd mode excitation circuit in Fig. 1c, the voltages and currents at the ports of the coupled sections can be specified as: $V_{1a} = V_{2b}$, $V_{2a} = V_{1b}$, $V_{3a} = V_{2c}$, $V_{4a} = V_{1c}$, $I_{1a} = -I_{2b}$, $I_{4a} = -I_{1c}$, $I_{2c} = -I_{3a} - \frac{V_{3a}}{Z_{swo}}$, $I_{4b} = I_{3c} = 0$, $V_{4c} = 0$, and $V_{3b} = -I_{3b}Z_{ro}$. Here, the input impedance of the switching path of $\mathrm{S_{W2}}$, $Z_{swo,SW2}$, will be same with (3a), while the input impedance for the switching path of $\mathrm{S_{W1}}$, $Z_{swo,SW1}$ can be expressed using (8):

$$Z_{swo,SW1} = j\mathrm{Z_{0sw}}\frac{\mathrm{Z_{0BS}}\tan(\theta_{BS}) + \mathrm{Z_{0sw}}\tan(\theta_{sw})}{\mathrm{Z_{0sw}} - \mathrm{Z_{0BS}}\tan(\theta_{BS})\tan(\theta_{sw})} \quad (8)$$

For the uncoupled sections, the input impedance Z_{ro} can be expressed using (9):

$$Z_{ro} = \mathrm{Z_{0r}}\frac{\mathrm{Z_{ro1}} + j\mathrm{Z_{0r}}\tan(\theta_{r1})}{\mathrm{Z_{0r}} + j\mathrm{Z_{ro1}}\tan(\theta_{r1})} \quad (9a)$$

$$Z_{ro1} = \frac{j\mathrm{Z_{0r}}\tan(\theta_{r2})}{1 - \omega C_{v1}\mathrm{Z_{0r}}\tan(\theta_{r2})}. \quad (9b)$$

As in the even mode excitation, the odd mode input impedance, Y_{odd}, can be similarly obtained by using (5) and (6) in (1). However, the expressions in (7a-7d) must be replaced with the following equations:

$$L_1 = -Z^b_{11} + \frac{(Z^b_{14})^2}{Z^b_{11} + Z_{ro}}, \quad L_2 = Z^b_{12} - \frac{Z^b_{13}Z^b_{14}}{Z^b_{11} + Z_{ro}} \quad (10a)$$

$$L_3 = -Z^b_{12} + \frac{Z^b_{13}Z^b_{14}}{Z^b_{11} + Z_{ro}}, \quad L_4 = Z^b_{11} - \frac{(Z^b_{13})^2}{Z^b_{11} + Z_{ro}} \quad (10b)$$

$$K_1 = Z^a_{11} - P_2, \quad K_2 = Z^a_{12} - P_3 \quad (10c)$$

$$K_3 = Z^a_{12} + Z^c_{12} - \frac{Z^c_{14}Z^c_{13}}{Z^c_{11}} - P_1P_2 \quad (10d)$$

$$K_4 = Z^a_{11} + Z^c_{11} - \frac{(Z^c_{14})^2}{Z^c_{11}} - P_1P_3 \quad (10e)$$

$$P_1 = \frac{Z^c_{13}Z^c_{14} - Z^c_{12}Z^c_{11}}{Z^c_{11}Z_{swo}} \quad (10f)$$

$$P_2 = \frac{\left[(Z^c_{13})^2 - (Z^c_{11})^2\right]Z_{swo}}{Z^c_{11}Z_{swo} + (Z^c_{11})^2 - (Z^c_{13})^2} \quad (10g)$$

$$P_3 = \frac{(Z^c_{13}Z^c_{14} - Z^c_{12}Z^c_{11})\,Z_{swo}}{Z^c_{11}Z_{swo} + (Z^c_{11})^2 - (Z^c_{13})^2}. \quad (10h)$$

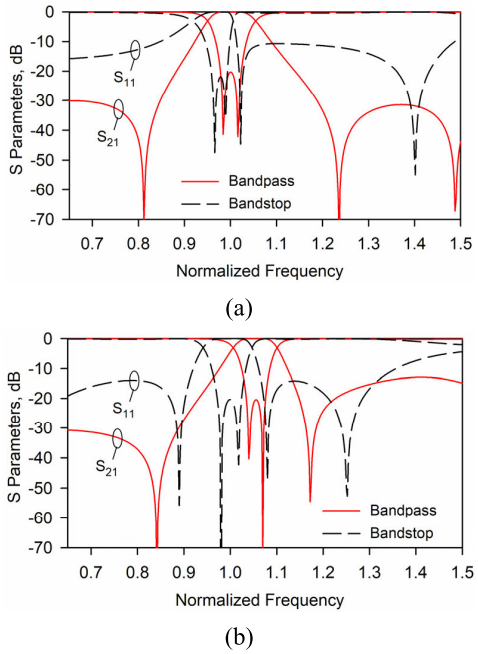

FIGURE 2. Bandpass-to-bandstop reconfigurability for the circuit schematic in Fig. 1. (a) $\theta_a = 33.8^0$, $\theta_b = 36^0$, $\theta_c = 40^0$, $\theta_{r1} = 0^0$, $\theta_{r2} = 45^0$, $\theta_{sw} = 45^0$, $\theta_{BS} = 9^0$, Z_{0e}= 129Ω Z_{0o}= 61.5 Ω, Z_{0sw}= 64Ω, Z_{0r}= 97.4Ω, Z_{0BS}= 40Ω, $C_{v1_{nor}}$=0.79x10^{-3}(*Bandpass mode*), $C_{v1_{nor}} = 0.98x10^{-3}$, (*Bandstopmode*), $C_{p_{nor}} = 0.705x10^{-3}$, *and* $C_{BP\_nor} = 10x10^{-3}$, (*b*)$\theta_a = 40^0$, $\theta_b = 18^0$, $\theta_c = 36^0$, $\theta_{r1} = 9^0$, $\theta_{sw} = 54^0$, $\theta_{BS} = 13.7^0$, $C_{v1_{nor}} = 0.65 \times 10^{-3}$(*Bandpass mode*), $C_{v1_{nor}} = 1.27x10^{-3}$(*Bandstop mode*), $C_{p_{nor}} = 0.8 \times 10^{-3}$.

Having defined the admittance relationships of the even and the odd mode circuit equivalent in (1), the overall S-parameters for each of the bandpass and the bandstop mode can be calculated using (11):

$$S_{21} = \frac{Y_0(Y_{even} - Y_{odd})}{(Y_0 + Y_{even})(Y_0 + Y_{odd})} \tag{11a}$$

$$S_{11} = \frac{Y_{even}Y_{odd} - Y_0^2}{(Y_0 + Y_{even})(Y_0 + Y_{odd})} \tag{11b}$$

where Y_0 is the input admittance. The overall S-parameters are plotted in Fig. 2(a) for the circuit parameters listed in the caption of Fig. 2(a). As it can be seen, the bandstop mode of operation exhibits a transfer function asymmetry. This is attributed to the transmission line sections being shared between the two modes of operation and optimized for a symmetric bandpass mode of operation. A symmetric bandstop mode of operation can also be obtained at the expense of a poor performance at the upper stopband as shown in Fig. 2(b). It should be noted that when generating the synthesized S-parameters in Fig. 2, the normalized capacitances need to be appropriately selected so that they can be implemented with realistic surface mounted devices (SMDs). In this implementation, the initial parameters are determined by optimization and using as a basis a targeted highest frequency of operation within the desired tuning range which is set equal to 2 GHz. For example, the normalized capacitors for the bandpass mode in Fig. 2(a) are $C_{v1\_nor} = 0.79x10^{-3}$,

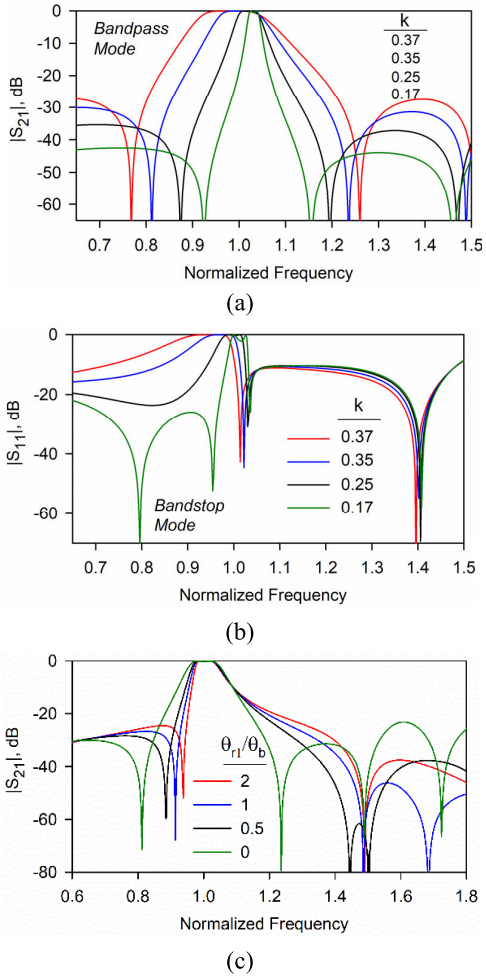

FIGURE 3. (a) Effects of the coupling coefficient on the frequency response of the bandpass mode. (b) Effects of the coupling coefficient on the frequency response of the bandstop mode. (c) Bandpass mode as the ratio θ_{r1}/θ_b is altered.

$C_{p\_nor} = 0.705x10^{-3}$, and $C_{BP\_nor} = 10x10^{-3}$ and their corresponding real values are $C_{v1} = 0.395\ pF, C_p = 0.35\ pF$, and $C_{BP} = 5\ pF$ at 2 GHz. For the bandstop mode of operation, C_{v1} is adjusted to 0.49 pF.

To determine the effect of the coupling strength $(k) = (Z_{0e} - Z_{0o})/(Z_{0e} + Z_{0o})$ between the DMLR and the feeding lines, S-parameters are investigated in Figs. 3(a) and 3(b) for the bandpass and the bandstop mode of operation with respect to the changes in k. It should be noted that the bandwidth can be enhanced with the increase of k. Furthermore, better out-band suppression can be achieved at both sides of the passband of the bandpass mode for lower k values. In the bandstop mode, the selectivity can be improved in the lower side of the stopband for lower k values, while the upper passband is almost unchanged. Fig. 3(c) illustrates the effects of the θ_{r1}/θ_b which affect the locations of the transmission zeros, which can be exploited to adjust the selectivity.

III. SINGLE-BAND BANDPASS-TO-BANDSTOP FILTER

Following the aforementioned design principles, a single-band bandpass-to-bandstop tunable filter can be designed

TABLE 1. Working principle of the filter.

V_1	V_2	SPDT1		SPDT2		Mode
		RF#1	RF#2	RF#1	RF#2	
High	Low	ON	OFF	OFF	ON	Bandstop
Low	High	OFF	ON	ON	OFF	Bandpass

using RF switches and varactor diodes as shown in the layout in Fig. 4(a). Initial dimensions are obtained using the analytical equations (1)-(10). The final dimensions are determined by parametric full-wave electromagnetic (EM) simulations in the software package SONNET. CEL's bidirectional pHEMT GaAs SPDT switches (CG2179M2) are used and DC blocking capacitors of 56 pF and DC bypass capacitors of 1000 pF are incorporated in the biasing network. Skyworks SMV2020-079LF varactor diode models are incorporated to represent the capacitors of C_{v1} and C_p. A close view of the switching region and equivalent circuit model of the varactor diodes are illustrated in Figs. 4(b) and 4(c), respectively. Operating principles of the filter are outlined in Table 1.

A parameter sweep process is performed for several of the physical dimensions of the filter including l_b, l_{BS}, l_{sw}, and w_c in order to obtain the best possible in-band performance while ensuring good out-band performance for both modes of operation. For the same, the position of the varactor diodes C_{v1} need also to be investigated as shown in Fig. 5. Although the varactor diodes of C_{v1} are placed after the transmission line with the electrical length of θ_{r1} in the aforementioned mathematical approach, it is also possible to shift them before this transmission line in the EM simulations. In this case, one more coupled section would occur and complexity of the mathematical approach would increase. As it can be seen in Fig. 5, the locations of these varactor diodes do not affect the type of transfer function. However, the horizontal distance to the corner, l_{cx}, and the vertical distance to the corner, l_{cy}, mostly affect the locations of the transmission zeros and the values of the varactor diodes.

For demonstration purposes, a single-band bandpass-to-bandstop filter was implemented and its photograph is shown in Fig. 6(a). A Rogers 4003C dielectric substrate with a dielectric constant of 3.55 and a thickness of 0.813 mm was used. The capacitor, C_{BP}, was selected as 6.2 pF for the best bandpass performance in terms of in-band return loss and out-band suppression. A DC block capacitor of $C_{DC\_v} = 8.2\ pF$ was used to isolate the varactor diodes and the bias resistors are $R_{bias} = 100k\Omega$. Final dimensions are $l_{sw} = 10.1$, $l_a = 8.8$, $l_b = 10.1$, $l_c = 6.3$, $l_{r1} = 3.1$, $l_{r2} = 14.0$, $l_{BS} = 3.6$, $w_{sw} = 1.2$, $w_r = 0.5$, $w_c = 1.2$, and $w_{BS} = 2.2$ mm. Besides, all gaps between the DMLR and the feeding network are 0.2 mm.

The implemented filter was measured using a Power Network Analyzer (PNA) N5222A from Keysight. Fig. 6(b) illustrates the EM-simulated and RF-measured tuning capabilities in the bandpass mode of operation, where V_1 and V_2 were set equal to 0V and 3V, respectively. As it shown, the center frequency can be tuned between 1.65 and 1.96 GHz by

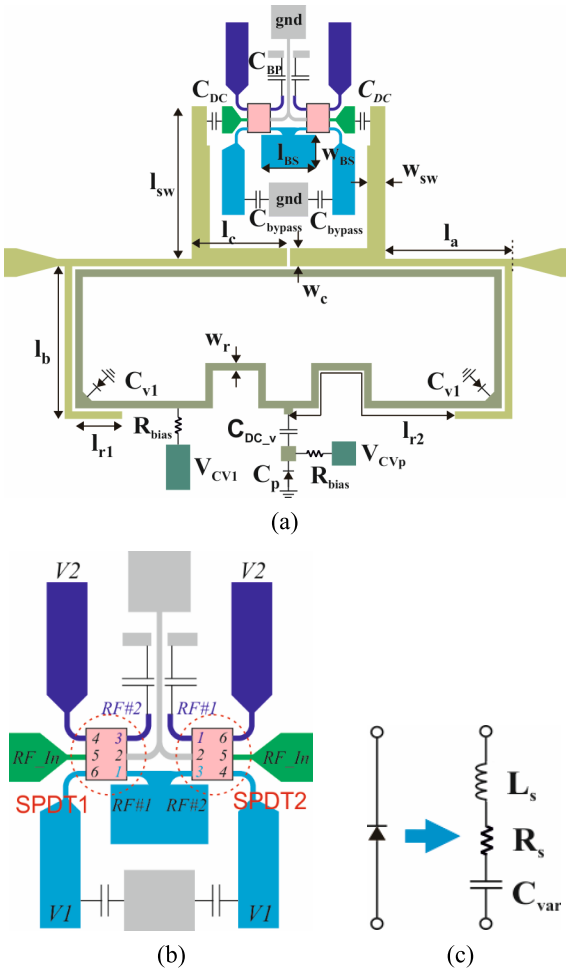

FIGURE 4. Single-band bandpass-to bandstop filter. (a) Layout. (b) Detail of the switching region and (c) the equivalent circuit model of the varactor diode ($L_s = 0.7\ nH$, $R_s = 2.5\Omega$, *Cvar*: Variable capacitance).

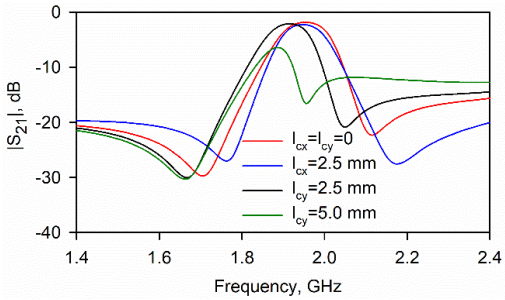

FIGURE 5. Effects of the locations of the varactor diodes on the frequency response.

altering the biasing on the varactor diodes. For these states the minimum insertion loss was measured between 7.1 dB and 2.8 dB and the 3-dB fractional bandwidth between 5.8 and 7.3 %. The minimum insertion loss is observed as 5.2 dB in the EM-simulations including the losses of conductors, varactor diodes and SPDT switches. It can be improved up to about 0.9 dB when the varactor diodes are lossless ($R_s = 0\ \Omega$). The measured insertion loss includes the losses of SMA connectors, varactor diodes, and SPDT switches. Fabrication errors and soldering process can also be effective

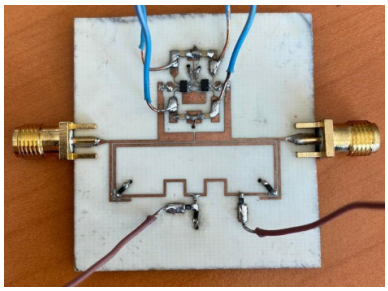

(a)

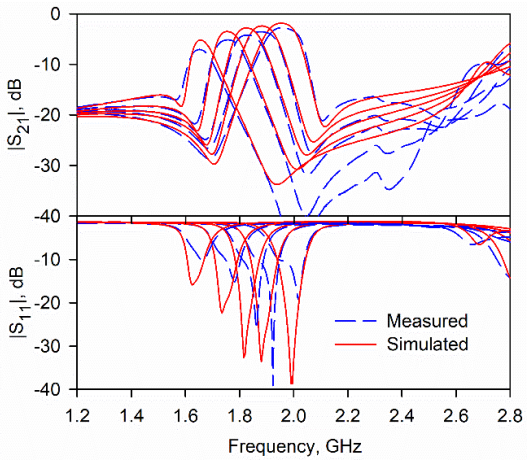

(b)

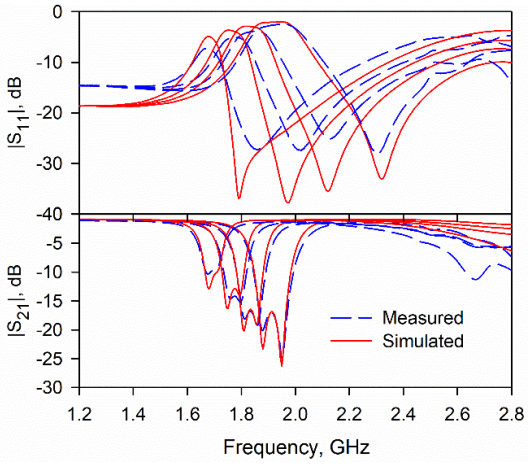

(c)

FIGURE 6. **(a) Photograph of the manufactured prototype of the single-band bandpass-to-bandstop filter. (b) EM-simulated and RF-measured performance of the bandpass mode. (c) EM-simulated and RF-measured performance of the bandstop mode.**

on the insertion loss. On the other hand, the filter can be reconfigured to the bandstop mode of operation by applying 3V and 0V to V_1 and V_2. In this case the center frequency can be tuned between 1.68 and 1.93 GHz, where the rejection levels are better than 10 dB.

IV. DUAL-BAND BANDPASS-TO-BANDSTOP FILTER DESIGN

To design the dual-band bandpass-to-bandstop filter, one more DMLR needs to be coupled to the feeding lines. However, this approach increases the complexity of mathematical analysis. Thus, the simplest way to design this filter is to first design two separate filters operating at different frequencies. After the initial dimensions are determined, both DMLRs need to be placed at the upper and bottom sides of the feeding lines as shown in Fig. 7. It should be noted that the switching network and bandpass-to-bandstop reconfiguration principle of the proposed filter is almost the same with the single-band filter in Fig. 4(b) and Table 1. However, C_{BP} is removed from the switching network to decrease the complexity and RF#2 of SPDT#1 and RF#1 of SPDT#2 are open-circuited. In this case, the input impedance in (3b) must be reconsidered as $Z_{swe,SW2} = -\mathrm{j}Z_{0\mathrm{sw}}\cot(\theta_{sw})$ to determine the initial dimensions. The filter can work in the bandstop mode when the outputs RF#1 of SPDT#1 and RF#2 of SPDT#2 are ON, while it is in the bandpass mode when the other RF output ports are ON.

The design steps for the dual-band bandpass-to-bandstop filter can be summarized as:

1. Determine the initial dimensions of both DMLRs separately for both of the required passbands using the mathematical model in Section II.
2. Construct the dual-band bandpass-to-bandstop filter based on the layout shown in Fig. 7.
3. Find the final dimensions for l_{b1}, l_{b2}, l_{r1}, l_{r2}, l_{r3}, and l_{r4} from the EM-simulated parameter sweeps so as to obtain the passbands at the highest center frequency of their tuning ranges. In this design, the highest center frequencies of the dual-band tunable bandpass-to-bandstop filter are aimed at 1.5 and 2 GHz.
4. Decide the desired in-band performance for the bandpass and bandstop modes of operation. The minimum insertion and return losses are aimed as better than 3 and 20 dB in the bandpass mode of operation. The in-band rejection level in the bandstop mode of operation is targeted as better than 20 dB.
5. Determine the final dimensions of l_{sw}, w_c, l_{BS}, and w_{BS} for the out-band performance in the bandpass and the bandstop modes of operation by means of EM-simulated parameter sweeps.
6. Decide the desired out-band performance for the bandpass and bandstop modes of operation. The out-band suppression in the bandpass mode of operation is desired to be better than 10 dB up to 1.5 f_0, where f_0 is the center frequency of the upper passband. The out-band return loss level in the bandstop mode of operation is also desired to be better than 10 dB up to 1.5 f_0.
7. Finish the design process after obtain the above response for both modes of operation.

The parameter sweep procedure for the dual-band bandpass-to-bandstop filter covering the steps between 3 and 6 is summarized in the flowchart shown in Fig. 8.

Having completed the parametric studies, a dual-band bandpass-to-bandstop filter was manufactured and tested.

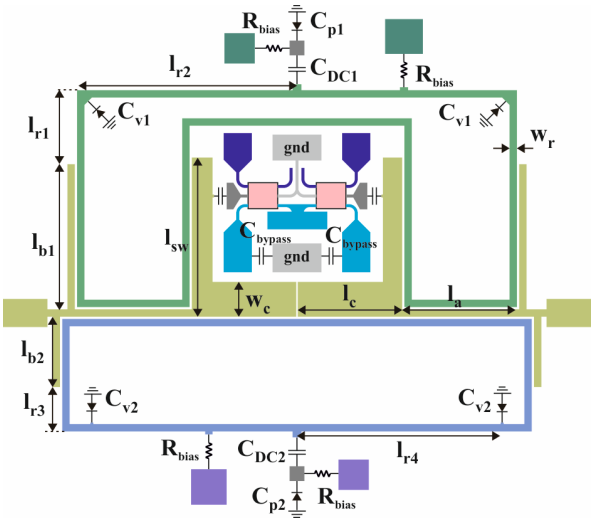

FIGURE 7. Layout of the dual-band bandpass-to-bandstop filter.

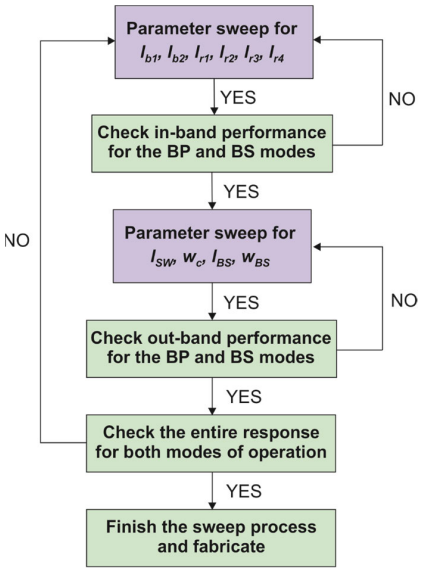

FIGURE 8. Design process flowchart for the dual-band bandpass-to-bandstop filter.

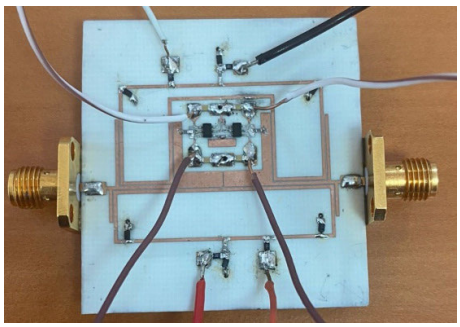

FIGURE 9. Photograph of the manufactured prototype of the dual-band bandpass-to-bandstop filter.

The photograph of the manufactured prototype is shown in Fig. 9. Likewise here, CEL's bidirectional pHEMT GaAs SPDT switches (CG2179M2) and Skyworks SMV2020-079LF varactor diodes were used in the prototype.

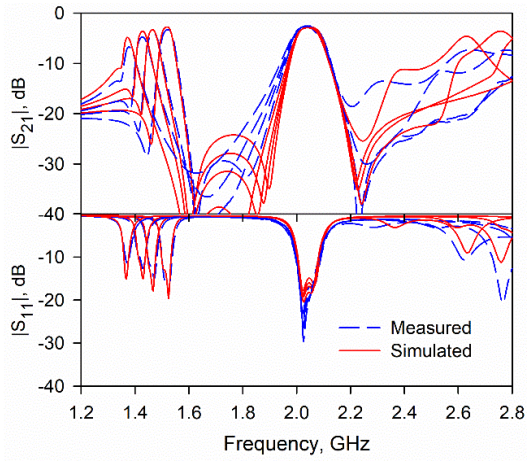

(a)

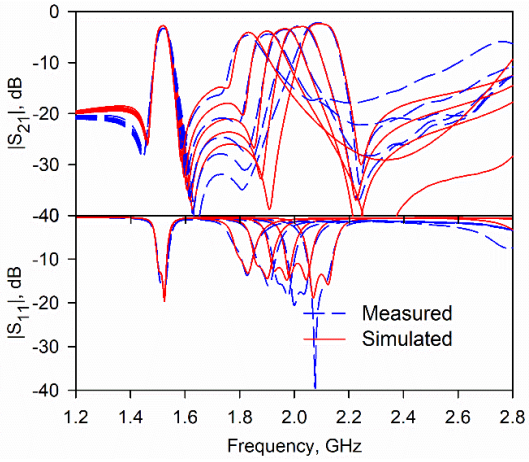

(b)

FIGURE 10. RF-measured and EM-simulated S-parameters of the dual-band bandpass-to-bandstop filter when reconfigured in its dual-band bandpass mode of operation. (a) Tuning of the low frequency band. (b) Tuning of the high frequency band.

Furthermore, DC block capacitors were employed to isolate the varactor diodes of C_p from C_{v1} and C_{v2} are $C_{DC1} = C_{DC2} = 8.2$pF. The final dimensions of the filter are l_{sw}= 10.75, l_a= 7.6, l_{b1}= 9.8, l_{b2}= 4.75, l_c= 7.05, l_{r1}= 5.0, l_{r2}= 14.85, l_{r3}= 3.0, l_{r4}= 15.85, l_{BS}= 4.05, w_{sw}= 1.4, w_r= 0.5, w_c= 2.35, w_{BS}= 1.2 and all gaps between the DMLR and the feeding network 0.15 mm.

The EM-simulated and RF-measured results in the bandpass mode of operation are compared in Figs. 10(a) and 10(b) and appear to be in a fair agreement. The first passband can be tuned by altering C_{v1} and C_{p1}, while the second passband can be tuned by changing C_{v2} and C_{p2}. In the EM-simulated bandpass mode of operation, C_{v1} and C_{p1} are adjusted from 0.35 pF to 0.93 pF, and 0.56 pF to 1.37 pF leading to a center frequency tuning between 1.37 and 1.53 GHz. Likewise, the second passband can be tuned between 1.82 and 2.1 GHz by adjusting C_{v2} between 0.38 and 0.8 pF, while C_{p2} is controlled between 0.63 and 1.53 pF. Fig. 10(a) depicts the tuning process of the first passband from 1.38 GHz to 1.53 GHz, where the RF-measured insertion loss varies between 3.3 and

TABLE 2. Comparison with some previous bandpass-to-bandstop filters.

	Passbands	BP IL	BS Rejection(dB)	BP Tuning Range	BS Tuning Range	Switching Technology	Size ($\lambda_g x \lambda_g$)
[26]	1	<4.3	>30	0.78-1.1	0.77-1.1	RF MEMS	-
[28]	2	<2.4/4.7	>15	No Tuning	No Tuning	RF MEMS	-
[32]	1	<5.9	>40	0.81-1.03	0.76-1.23	PIN Diodes	0.258x0.219
[35]	2	<5.0/5.6	>16.4/20	1.7-2.2/ 2.2-2.7	1.7-2.3/ 2.3-2.9	PIN Diodes	0.33x0.34
[36]	2	<2.6/3.1	>11/11	1.03-1.4/ 1.35-1.74	1-1.5/ 1.4-1.75	PIN Diodes	-
[42]	1	0.86	>40	No Tuning (Wideband)	No Tuning (Wideband)	SPDT RF Switches	-
[44]	1	<5.4	>35	1.9-2.45	2.6-2.9	SPDT RF Switches	-
This Work	1	<7.1	>10	1.65-1.96	1.68-1.93	SPDT RF Switches	0.33x0.28
	2	<6.8/4.7	>10/10	1.38-1.53/ 1.82-2.08	1.35-1.47/ 1.75-2.01		0.25x0.26

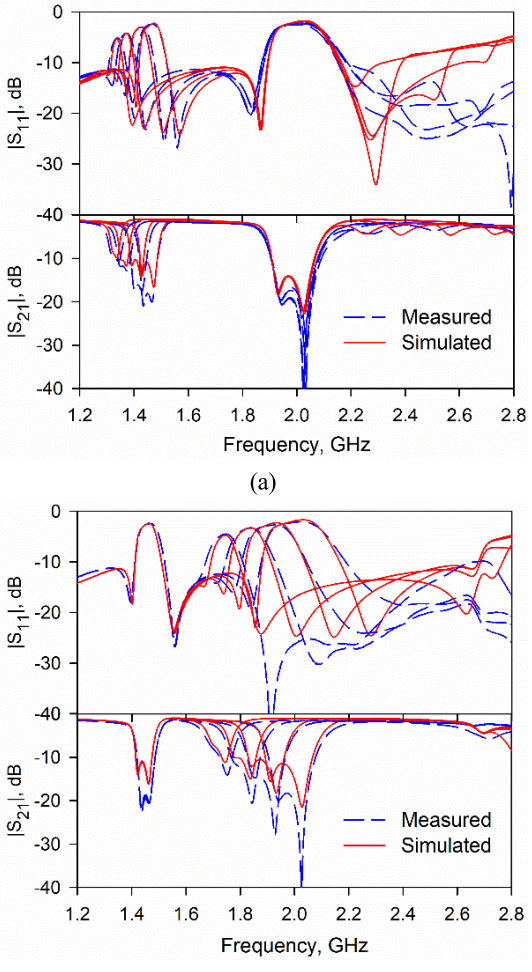

FIGURE 11. RF-measured and EM-simulated S-parameters of the dual-band bandpass-to-bandstop filter when reconfigured in its dual-band bandstop mode of operation. (a) Tuning of the low frequency band. (b) Tuning of the high frequency band.

6.8 dB. Within the tuning range, the 3-dB fractional bandwidth changes between 2.9 and 3.9 %. It is clear that the first passband can be independently tuned, while the second passband is almost fixed. However, depending on the second harmonic of the first band, the upper stopband of the second passband cannot be kept constant. The tuning process for the second passband is illustrated in Fig. 10(b) alongside a comparison between the RF-measured and EM- simulated parameters. The center frequency of the second passband can be tuned between 1.82 and 2.08 GHz. Within this tuning range, the 3-dB fractional bandwidth is kept between 6 and 6.5 %, and the insertion loss varies between 2.2 and 4.7 dB. It should be noted that both passbands can be independently tuned. In the EM-simulations, the minimum insertion losses are better than 5 and 4.5 dB, while they can be improved up to 2.5 and 1.6 dB when the varactor diodes are lossless (R_s =0 Ω). When taking into account the use of six varactor diodes and two SPDT switches, the measured insertion losses of the passbands can be considered as natural.

The tuning capabilities of the bandstop mode of operation ($V_1 = 3V$ and $V_2 = 0V$) are shown in Figs. 11(a) and 11(b) for the first and second stopband, respectively. In the EM-simulated bandstop mode of operation, C_{v1} and C_{p1} are adjusted from 0.39 pF to 0.95 pF, and 1.015 pF to 1.8 pF leading to a center frequency tuning between 1.36 and 1.46 GHz. Likewise, the second stopband can be tuned between 1.75 and 1.97 GHz by adjusting C_{v2} between 0.38 and 0.85 pF, while C_{p2} is controlled between 1.1 and 2 pF. Center frequency of the first stopband can be tuned from 1.35 GHz to 1.47 GHz, where the 3-dB fractional bandwidth varies between 4.4 and 5.4 % as shown in Fig. 11(a). Within this tuning range, the measured minimum in-band return loss changes from 5.2 dB to 2.5 dB. The out-band return loss levels were measured as better than 10 dB within the given frequency spectrum. The EM-simulated and RF-measured results for the tunability of the second stopband are illustrated in Fig. 11(b). The tuning range of the second stopband was measured as 1.75-2.01 GHz, where the corresponding 3-dB bandwidth changes between 5.7 and 10.9 %. Here, the return loss was measured between 4.5 and 2.1 dB, while the rejection levels at the center frequencies are always better than 10 dB. In all RF-measurements, the out-band return loss performance was measured less than 10 dB.

Table 2 represents the comparison of the proposed bandpass-to-bandstop DMLR-based concept with state-of-the-art tunable and reconfigurable RF filters. As compared to the single-band bandpass-to-bandstop filters introduced in [26], [32], [42], and [44], the proposed work stands out in

terms of dual-band performance characteristics. Among dual-band bandpass-to-bandstop filters, it is advantageous when compared to the concept in [28] due to [28] being static. Although there are few dual-band electronically tunable bandpass-to-bandstop filters constructed by PIN diodes [35] and [36], to the best of authors' knowledge, the dual-band bandpass-to-bandstop filter in this work is the first among SPDT based tunable bandpass-to-bandstop filters. The switching mechanism consists of two SPDT switches and their bias circuits arranged within a small space in a similar manner with RF filter banks. Therefore, the proposed topology can be improved more as a bandpass-to-bandstop RF filter bank to obtain wider tuning ranges or different transfer functions. Furthermore, the overall size of the proposed dual-band tunable bandpass-to-bandstop filter is better than that of the filter in [35]. Although the filters in [35] and [36] exhibit good in-band performance, they suffer from their poor out-band return loss performance in their bandstop mode of operation.

V. CONCLUSION

A new class of single- and dual-band frequency-tunable bandpass-to-bandstop filters has been introduced in this paper. The bandpass-to-bandstop switching operation has been realized by incorporating two reciprocally located commercial SPDT switches. Thus, the design methodology of the proposed tunable bandpass-to-bandstop filters is in a similar manner with RF filter banks. Therefore, the proposed approach can potentially be improved by incorporating SP3T or SP4T switches in order to widen the tuning ranges or to achieve different transfer functions. The single-band filter can be constructed by coupling a DMLR to the feeding lines that are connected to the RF input and output ports, while the dual-band filter is designed by coupling two DMLRs having different electrical lengths. Center frequency tunability for both of the single- and dual-band filter topologies has been achieved by three varactor diodes located at the DMLRs. For experimental validation purposes, two filters with single- and dual-band responses were implemented and tested and are in a good agreement with the EM-simulated performance. The RF-measured tuning ranges of the bandpass and bandstop modes of operation for the single-band filter were measured as 1.65-1.96 GHz and 1.68-1.93 GHz. For the bandpass mode of the dual-band filter prototype, the RF-measured tuning ranges of its bands were measured as 1.38-1.53 GHz and 1.82-2.08 GHz. For the bandstop mode they were measured as 1.35-1.47 GHz and 1.75-2.01 GHz.

REFERENCES

[1] A. K. Gorur, C. Karpuz, and A. Gorur, "Design of dual-mode dual-band bandpass filter with independently tunable bandwidths and reconfigurable filtering characteristics," in *IEEE MTT-S Int. Microw. Symp. Dig.*, Honolulu, HI, USA, Jun. 2017, pp. 922–925.

[2] M. Ohira, S. Hashimoto, and Z. Ma, "A new microstrip reconfigurable transversal coupling bandpass filter with highly controllable number and positions of transmission zeros," in *Proc. IEEE Asia-Pacific Microw. Conf. (APMC)*, Dec. 2019, pp. 1706–1708.

[3] N. Kumar, S. Narayana, and Y. K. Singh, "Constant absolute bandwidth tunable symmetric and asymmetric bandpass responses based on reconfigurable transmission zeros and bandwidth," *IEEE Trans. Circuits Syst. II, Exp. Briefs*, vol. 69, no. 3, pp. 1014–1018, Mar. 2022.

[4] A. K. Gorur, E. Dogan, C. Karpuz, and A. Gorur, "Design of tunable microstrip diplexer with reconfigurable filtering characteristics based on dual-mode square loop resonators," *IET Microw., Antennas Propag.*, vol. 14, no. 13, pp. 1587–1594, Sep. 2020.

[5] D. J. Simpson, R. Gómez-García, and D. Psychogiou, "Single-/multi-band bandpass filters and duplexers with fully reconfigurable transfer-function characteristics," *IEEE Trans. Microw. Theory Techn.*, vol. 67, no. 5, pp. 1854–1869, May 2019.

[6] H. Jiang, B. Lacroix, and J. Papapolymerou, "Compact tunable UHF bandstop resonator filter using varactor-loaded CPW bottom-side meander line," in *Proc. 41st Eur. Microw. Conf.*, Manchester, U.K., Oct. 2011, pp. 1063–1066.

[7] N. Zhang, Z. Deng, and F. Sen, "CPW tunable band-stop filter using hybrid resonator and employing RF MEMS capacitors," *IEEE Trans. Electron Devices*, vol. 60, no. 8, pp. 2648–2655, Aug. 2013.

[8] D. Psychogiou and R. Gómez-García, "Reflectionless adaptive RF filters: Bandpass, bandstop, and cascade designs," *IEEE Trans. Microw. Theory Techn.*, vol. 65, no. 11, pp. 4593–4605, Nov. 2017.

[9] P.-Y. Qin, F. Wei, and Y. J. Guo, "A wideband-to-narrowband tunable antenna using a reconfigurable filter," *IEEE Trans. Antennas Propag.*, vol. 63, no. 5, pp. 2282–2285, May 2015.

[10] F. Wei, C. Y. Zhang, C. Zeng, and X. W. Shi, "A reconfigurable balanced dual-band bandpass filter with constant absolute bandwidth and high selectivity," *IEEE Trans. Microw. Theory Techn.*, vol. 69, no. 9, pp. 4029–4040, Sep. 2021.

[11] R. Gómez-García and A. C. Guyette, "Reconfigurable multi-band microwave filters," *IEEE Trans. Microw. Theory Techn.*, vol. 63, no. 4, pp. 1294–1307, Apr. 2015.

[12] M. R. A. Nasser and D. Psychogiou, "Acoustic wave resonator-based bandpass filters with continuously tunable fractional bandwidth," *IEEE Trans. Circuits Syst. II, Exp. Briefs*, vol. 70, no. 4, pp. 1390–1394, Apr. 2023.

[13] D. Psychogiou, R. Gómez-García, and D. Peroulis, "Tunable acoustic-wave-lumped-element resonator (AWLR)-based bandpass filters," in *IEEE MTT-S Int. Microw. Symp. Dig.*, San Francisco, CA, USA, May 2016, pp. 1–4.

[14] D. Psychogiou, R. Gómez-García, R. Loeches-Sánchez, and D. Peroulis, "Hybrid acoustic-wave-lumped-element resonators (AWLRs) for high-Q bandpass filters with quasi-elliptic frequency response," *IEEE Trans. Microw. Theory Techn.*, vol. 63, no. 7, pp. 2233–2244, Jul. 2015.

[15] D. Psychogiou and D. J. Simpson, "Multi-band acoustic-wave-lumped-element resonator-based bandstop filters with continuously tunable stopband bandwidths," in *IEEE MTT-S Int. Microw. Symp. Dig.*, Philadelphia, PA, USA, Jun. 2018, pp. 860–863.

[16] M. Inaba, K.-Y. Hashimoto, T. Omori, and C. Ahn, "A widely tunable filter configuration composed of high q RF resonators and variable capacitors," in *Proc. Eur. Microw. Integr. Circuit Conf.*, Nuremberg, Germany, Oct. 2013, pp. 320–323.

[17] M. Kadota, M. Esashi, S. Tanaka, Y. Ida, and T. Kimura, "Improvement of insertion loss of band pass tunable filter using SAW resonators and GaAs diode variable capacitors," in *Proc. IEEE Int. Ultrason. Symp. (IUS)*, Prague, Czech Republic, Jul. 2013, pp. 1668–1671.

[18] T. Wada, T. Ogami, A. Horita, H. Obiya, M. Koshino, M. Kawashima, and N. Nakajima, "A new tunable SAW filter circuit for reconfigurable RF," in *IEEE MTT-S Int. Microw. Symp. Dig.*, San Francisco, CA, USA, May 2016, pp. 1–4.

[19] A. Perigaud, O. Tantot, N. Delhote, S. Bila, S. Verdeyme, and D. Baillargeat, "Continuously tunable filter made by additive manufacturing using a 3D spiral ribbon," in *IEEE MTT-S Int. Microw. Symp. Dig.*, Pavia, Italy, Sep. 2017, pp. 1–3.

[20] A. Olaru, N. Delmonte, S. Marconi, G. Alaimo, F. Auricchio, and M. Bozzi, "Tunable microwave filter based on hemispherical 3D-printed resonators," in *Proc. 24th Int. Microw. Radar Conf. (MIKON)*, Gdansk, Poland, Sep. 2022, pp. 1–4.

[21] D. Psychogiou and M. Deng, "High-order coaxial bandpass filters with multiple levels of transfer function tunability," *IEEE Microw. Wireless Compon. Lett.*, vol. 30, no. 4, pp. 367–370, Apr. 2020.

[22] K. Sadasivan and D. Psychogiou, "Tunable 3D-printed coaxial-cavity filters with mixed electromagnetic coupling," in *Proc. IEEE Int. Symp. Antennas Propag. USNC-URSI Radio Sci. Meeting*, Atlanta, GA, USA, Jul. 2019, pp. 1703–1704.
[23] A. Dyussembayev and D. Psychogiou, "Continuously tunable 3-D printed helical resonators and bandpass filters using actuated liquid metals," *IEEE Microw. Wireless Compon. Lett.*, vol. 32, no. 7, pp. 855–858, Jul. 2022.
[24] R. Stefanini, M. Chatras, A. Pothier, C. Guines, and P. Blondy, "High-Q 3D tunable RF MEMS filter with a constant fractional bandwidth," in *Proc. Eur. Microw. Integr. Circuit Conf.*, Nuremberg, Germany, Oct. 2013, pp. 312–315.
[25] Y.-H. Cho and G. M. Rebeiz, "0.7–1.0-GHz reconfigurable bandpass-to-bandstop filter with selectable 2- and 4-pole responses," *IEEE Trans. Microw. Theory Techn.*, vol. 62, no. 11, pp. 2626–2632, Nov. 2014.
[26] Y.-H. Cho and G. M. Rebeiz, "Two- and four-pole tunable 0.7–1.1-GHz bandpass-to-bandstop filters with bandwidth control," *IEEE Trans. Microw. Theory Techn.*, vol. 62, no. 3, pp. 457–463, Mar. 2014.
[27] T. Yang and G. M. Rebeiz, "Bandpass-to-bandstop reconfigurable tunable filters with frequency and bandwidth controls," *IEEE Trans. Microw. Theory Techn.*, vol. 65, no. 7, pp. 2288–2297, Jul. 2017.
[28] N. Kumar and Y. K. Singh, "RF-MEMS-based bandpass-to-bandstop switchable single- and dual-band filters with variable FBW and reconfigurable selectivity," *IEEE Trans. Microw. Theory Techn.*, vol. 65, no. 10, pp. 3824–3837, Oct. 2017.
[29] Y. Zhu and Y. Dong, "Novel dual-band bandpass-to-bandstop filter using shunt PIN switches loaded on the transmission line," in *IEEE MTT-S Int. Microw. Symp. Dig.*, Los Angeles, CA, USA, Aug. 2020, pp. 924–927.
[30] M. K. Zahari, B. H. Ahmad, P. W. Wong, and N. A. Shairi, "Switchable bandstop to bandpass filter using parallel-coupled resonator," in *Proc. IEEE Asia-Pacific Microw. Conf. (APMC)*, Kuala Lumpur, Malaysia, Nov. 2017, pp. 513–516.
[31] M. Fan, K. Song, Y. Zhu, and Y. Fan, "Compact bandpass-to-bandstop reconfigurable filter with wide tuning range," *IEEE Microw. Wireless Compon. Lett.*, vol. 29, no. 3, pp. 198–200, Mar. 2019.
[32] R. Li and F. Chen, "A tunable bandpass-to-bandstop filter with controllable bandwidth and high rejection level," *Microw. Opt. Technol. Lett.*, vol. 59, no. 1, pp. 110–113, Jan. 2017.
[33] K. Song, W. Chen, S. R. Patience, Y. Chen, A. M. Iman, and Y. Fan, "Compact wide-frequency tunable filter with switchable bandpass and bandstop frequency response," *IEEE Access*, vol. 7, pp. 47503–47508, 2019.
[34] D. J. Simpson, R. Gómez-García, and D. Psychogiou, "Tunable multiband bandpass-to-bandstop RF filters," in *IEEE MTT-S Int. Microw. Symp. Dig.*, Philadelphia, PA, USA, Jun. 2018, pp. 1363–1366.
[35] F.-C. Chen, R.-S. Li, and J.-P. Chen, "A tunable dual-band bandpass-to-bandstop filter using p-i-n diodes and varactors," *IEEE Access*, vol. 6, pp. 46058–46065, 2018.
[36] S. Narayana and Y. K. Singh, "Dual-band bandpass to bandstop switchable filter with independently tunable center frequency and bandwidth," *Microw. Opt. Technol. Lett.*, vol. 63, no. 11, pp. 2704–2709, Nov. 2021.
[37] S. Kingsly, M. Kanagasabai, M. G. N. Alsath, A. K. Shrivastav, S. Subbaraj, Y. P. Selvam, R. Sivasamy, and Y. V. Ramanarao, "Compact frequency and bandwidth tunable bandpass–bandstop microstrip filter," *IEEE Microw. Wireless Compon. Lett.*, vol. 28, no. 9, pp. 786–788, Sep. 2018.
[38] S. Kingsly, M. Kanagasabai, M. G. N. Alsath, S. Subbaraj, S. K. Palaniswamy, and B. Bhuvaneswari, "Switchable resonator based reconfigurable bandpass/bandstop microstrip filter," *Int. J. Electron.*, vol. 108, no. 9, pp. 1610–1622, Apr. 2021.
[39] R. Gómez-García, L. Yang, J.-M. Muñoz-Ferreras, and D. Psychogiou, "Single/multi-band coupled-multi-line filtering section and its application to RF diplexers, bandpass/bandstop filters, and filtering couplers," *IEEE Trans. Microw. Theory Techn.*, vol. 67, no. 10, pp. 3959–3972, Oct. 2019.
[40] M. K. Zahari, B. H. Ahmad, W. P. Wen, and N. A. Shairi, "Switchable absorptive bandstop to bandpass filter using dual-mode ring resonator," in *Proc. IEEE Asia-Pacific Conf. Appl. Electromagn. (APACE)*, Langkawi, Malaysia, Dec. 2016, pp. 248–251.
[41] T.-H. Lee, J.-J. Laurin, and K. Wu, "Reconfigurable filter for bandpass-to-absorptive bandstop responses," *IEEE Access*, vol. 8, pp. 6484–6495, 2020.
[42] S. Arain, P. Vryonides, K. Nisar, A. Quddious, and S. Nikolaou, "Novel selective feeding scheme integrated with SPDT switches for a reconfigurable bandpass-to-bandstop filter," *IEEE Access*, vol. 9, pp. 25233–25244, 2021.
[43] N. S. Luhrs, D. J. Simpson, and D. Psychogiou, "Multiband acoustic-wave-lumped-element resonator-based bandpass-to-bandstop filters," *IEEE Microw. Wireless Compon. Lett.*, vol. 29, no. 4, pp. 261–263, Apr. 2019.
[44] T. Yang and G. M. Rebeiz, "A 1.9–2.6 GHz filter with both bandpass-to-bandstop reconfigurable function and bandpass-and-bandstop cascading function," in *IEEE MTT-S Int. Microw. Symp. Dig.*, Honolulu, HI, USA, Jun. 2017, pp. 264–266.
[45] D. M. Pozar, *Microwave Engineering*, 3rd ed, New York, NY, USA: Wiley, 2003.

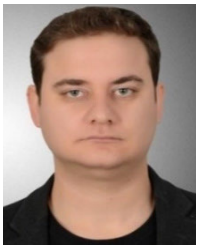

ALI KURSAD GORUR (Member, IEEE) was born in Kayseri, Türkiye, in 1986. He received the B.Sc. degree in electrical and electronics engineering from Hacettepe University, Türkiye, in 2009, and the M.Sc. and Ph.D. degrees in electrical and electronics engineering from Pamukkale University, Türkiye, in 2011 and 2016, respectively. From 2011 to 2016, he was with the Department of Electrical and Electronics Engineering, Pamukkale University, as a Research Assistant. In 2016, he joined the Department of Electrical and Electronics Engineering, Nevşehir Hacı Bektaş Veli University, Türkiye, as an Assistant Professor, where he was an Associate Professor, from 2018 to 2024, and has been a Professor, since 2024. His current research interests include tunable/multi-band planar filters, multiplexers, balun bandpass filters, filtering power dividers for wireless communication systems, and chipless RFID tags.

DIMITRA PSYCHOGIOU (Senior Member, IEEE) received the Dipl.-Eng. degree in electrical and computer Engineering from the University of Patras, Patras, Greece, in 2008, and the Ph.D. degree in electrical engineering from the Swiss Federal Institute of Technology (ETH), Zürich, Switzerland, in 2013. She is currently a Professor of electrical and electronic engineering with the University College Cork (UCC) and the Head of the Advanced RF Technology Group, Tyndall National Institute, Cork, Ireland. Prior to joining UCC, she was a Senior Research Scientist with Purdue University, West Lafayette, IN, USA, and an Assistant Professor with the University of Colorado Boulder, Boulder, CO, USA. Her research has been presented in more than 250 publications. Her current research interests include RF design and characterization of reconfigurable microwave and millimeter-wave passive components, RF-MEMS, acoustic wave resonator-based filters, tunable filter synthesis, frequency-agile antennas, and additive manufacturing technologies for 3D antenna sub-systems. She is a Senior Member of URSI and a member of the IEEE MTT-S Filters and Passive Components (MTT-5) and Microwave Control Materials and Devices (MTT-13) committees. She has received the 2023 IEEE MTT-S Outstanding Young Engineer Award, the 2021 Roberto Sorrentino Prize, the SFI Research Professorship Award, the 2020 NSF CAREER Award, the 2020 URSI Young Scientist Award, and the Junior Faculty Outstanding Research Award from UC Boulder. Her students have also received numerous student-paper awards and research-based fellowships. She is currently serving as the President of URSI Ireland, the Vice-Chair of MTT-13, and the Secretary of USNC-URSI Commission D. She is also an Associate Editor of IEEE Microwave and Wireless Components Letters and *International Journal of Microwave and Wireless Technologies*. She is on the Technical Review Board of various IEEE and EuMA conferences. Previously, she was an Associate Editor of the *IET Microwaves, Antennas and Propagation journal*.